1   **Structural insight into binding site access and ligand recognition by human ABCB1**

2

3   **Devanshu Kurre[1], Phuoc X. Dang[1,2], Le T.M. Le[1,3], Varun V. Gadkari[4], and Amer Alam[1#]**

4   [1] The Hormel Institute, University of Minnesota, Austin, Minnesota 55912, United States

5   [2]Current Address: Department of Pharmacy - Inpatient, Mayo Clinic, Rochester, Minnesota 55901,

6   United States

7   [3]Current Address: Department of Biochemistry and Molecular Biology, Mayo Clinic, Rochester,

8   Minnesota 55901, United States

9   [4]Department of Chemistry, University of Minnesota, Minneapolis, Minnesota 55455, United

10   States

11   [#]Address correspondence to: aalam@umn.edu

12   **Abstract:**

13   ABCB1 is a broad-spectrum efflux pump central to cellular drug handling and multidrug resistance

14   in humans. However, its mechanisms of poly-specific substrate recognition and transport remain

15   poorly resolved. Here we present cryo-EM structures of lipid embedded human ABCB1 in its apo,

16   substrate-bound, inhibitor-bound, and nucleotide-trapped states at 3.4-3.9 Å resolution without

17   using stabilizing antibodies or mutations and each revealing a distinct conformation. The substrate

18   binding site is located within one half of the molecule and, in the apo state, is obstructed by

19   transmembrane helix (TM) 4. Substrate and inhibitor binding are distinguished by major

20   differences in TM arrangement and ligand binding chemistry, with TM4 playing a central role in

21   all conformational transitions. Our data offer fundamental new insights into the role structural

22   asymmetry, secondary structure breaks, and lipid interactions play in ABCB1 function and have

23   far-reaching implications for ABCB1 inhibitor design and predicting its substrate binding profiles.

24   **Introduction**

25   The ATP binding cassette (ABC) transporter ABCB1, also known as Multidrug resistance

26   protein (MDR)1 or P-glycoprotein (p-gp) is a ubiquitously expressed drug exporter that plays a

27   key role in cellular drug handling[1-8]. Its pharmacological relevance makes it a key transporter in

28   the Food and Drug Administration's guidance for all developmental drugs to be screened against[10].

29   ABCB1 activity can be a limiting factor in cancer chemotherapy [6,11-14] and treatment of

30   neurological disorders[4,15-19] and has been increasingly implicated in accumulation of amyloid-beta

31   peptides, a hallmark feature of Alzheimer's Disease[17]. Despite its relevance, ABCB1's promise as

32   druggable clinical target remains unrealized largely due to systemic toxicities and off target effects

33   resulting from its inhibition[14,20]. Understanding the detailed mechanisms by which ABCB1

34   recognizes and transports a wide range of structurally and chemically diverse substrates remains a

35   major focus in biomedicine. Visualizing the underlying chemistry involved is key to designing

36   more specific ABCB1 inhibitors and circumventing ABCB1 mediated efflux of a wide range of

37   developmental drugs. However, despite long-term efforts, ABCB1 has so far remained notoriously

38   averse to direct structural analysis without the use of antibody fragments and stabilizing mutations

39   to aid conformational trapping.

40   ABCB1 is a type II ABC exporter/type IV ABC transporter with each TMD comprising 6

41   transmembrane helices (TMs) and followed by a cytosolic nucleotide binding domain (NBD). It

42   is topologically arranged as a pseudo-symmetric domain swapped dimer with the 4th and 5th TMs

43   of each TMD making extensive contacts with the opposing TMDs and NBDs as first revealed by

44   the structure of its bacterial homolog Sav1866[22]. To date, the only structures of human ABCB1

45   determined are those of its hydrolysis deficient mutant in the ATP bound outward facing (OF)

46   state and those in complex with antigen binding fragments (Fabs) from the inhibitory antibodies

47   UIC2[23] and MRK16[24]. Key mechanistic questions about polyspecific substrate recognition and the

48   drug transport cycle of ABCB1 therefore remain open. First, the nature of its Inward Facing (IF)

49   apo state remains unknown, leaving open the question of show substrates gain access to their

50   respective binding site(s). Second, the binding chemistry governing differential substrate and

51   inhibitor interactions with ABCB1 in the absence of conformational trapping by inhibitory Fabs

52   remains unknown. Third, it is unclear what role sequence and structural asymmetry plays in

53   ABCB1 function. Finally, while lipids have been implicated in modulation of ABCB1 structure

54   and its interaction with ligands [25-28], the extent and specifics of these interactions remains largely

55   unexplored.

56   To address the above-mentioned gaps in knowledge, we determined multiple structures of

57   wildtype human ABCB1 in a lipid environment by single particle cryo-EM. Four distinct

58   conformations of the transporter were observed including, for the first time, its IF apo and

59   substrate-bound states. These structures allow us to map out the conformational transitions

60   associated with ligand and nucleotide binding and visualize key differences in how substrates and

61   inhibitors interact with the TMD. They highlight the concerted TM and NBD movements

62   underlying ATP coupled drug transport and regulation of binding site access and the complex

63   interplay between lipid interactions and TM secondary structure breaks that impart tremendous

64   TMD flexibility and overall conformational heterogeneity to human ABCB1 that has made its

65   high-resolution structure determination difficult. Overall, our results offer fundamental insights

66   into the mechanistic details of the ABCB1 drug transport cycle and its inhibition that will have

67   significant implications for ABCB1 targeted therapeutic design in various medical applications as

68   well broader drug-development efforts where potential ABCB1 interactions may limit drug-

69   bioavailability, among other undesired effects.

Four distinct conformations of lipid-embedded wildtype human ABCB1

71   Human ABCB1 (ABCB1) was stably expressed in HEK293 cells, purified in detergent, and

72   reconstituted in saposin A (sapA) nanoparticles comprising a mixture of Brain Polar Lipids (BPL)

73   and cholesterol (Chol). SapA reconstituted ABCB1 displayed a more homogenous mass

74   distribution as analyzed by native mass spectrometry (nMS) as well as greater ATPase activity

75   compared to MSP1D1 nanodisc reconstituted samples (Figure 1A-B) and was chosen for cryo-EM

76   analysis. We analyzed ABCB1 in its apo state and in the presence of ATP/Mg^{2+} and either the

77   substrate Taxol, representing turnover conditions similar to a recent analysis for human ABCG2[29],

78   or its third-generation inhibitor Zosuquidar. Taxol and Zosuquidar complexes of ABCB1 in the

79   absence of ATP/Mg^{2+} displayed near identical conformations and are not discussed in further detail

80   here. We also determined the structure of its nucleotide trapped state in the presence of ATPγS,

81   allowing for a visualization of the conformational spectrum associated with the drug transport

82   cycle and its inhibition in ABCB1 (Figure 1C). The overall conformation of the zosuquidar

83   complex was nearly identical to the inhibitor occluded state seen in the presence of UIC2 or

84   MRK16 fabs[23,24]. Similarly, the ATPγS trapped ABCB1 structure was identical to that previously

85   reported for ATP bound state of its hydrolysis deficient EQ mutant in a detergent environment [30].

86   In contrast, the conformations observed for its apo- and substrate bound states are fundamentally

87   different and has not been previously described. Conventional models of the apo state of ABCB1

88   based on homologous structures or alphafold predictions invoke a symmetric, IF conformation

89   with a wide separation between the NBDs as seen in the crystal structure of murine ABCB1[31].

90   Substrate binding is thought to promote NBD closure and explain consequent ATPase rate

91   stimulation. In contrast, the apo state structure determined here displays distinct asymmetry

92   between the two halves and closely spaced NBDs while the Taxol complex shows an IF_{OPEN} state

93   with wider NBD separation compared to the apo conformation, among other significant differences

94   compared to structures of the Taxol- complex of ABCB1 bound to inhibitory antibodies, as

95   discussed in detail below.
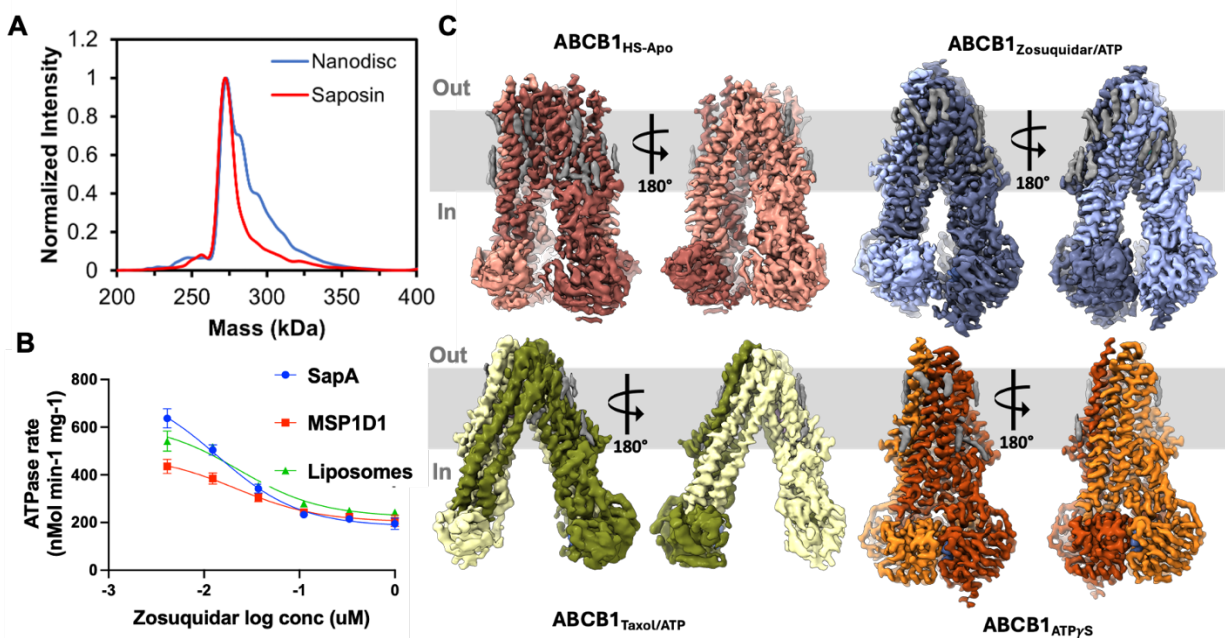
Figure 1 Conformational landscape of lipid embedded human ABCB1. A Comparison of saposin and nanodisc reconstituted human ABCB1 by nMS B) Comparison of ATPase activity of saposin, MSP1D1 nanodisc, and Liposome reconstituted human ABCB1. n=3 and error bars denote standard deviation. C Structures of human ABCB1 in multiple distinct conformational states. EM density for the two halves is colored differently and that of modeled acyl chains is colored gray.

96   **Apo ABCB1 adopts a unique IF_{CLOSED} conformation**

97   The predominant conformation of apo ABCB1 observed here features an asymmetric TMD

98   arrangement with a closed central TMD pathway (Figure 2A), closely spaced NBDs, and widely

99   spaced extracellular "wings"[22] (Figure 1C). We chose to classify this state as an IF_{CLOSED} state

100   based on TMD conformation. The structure is marked by multiple secondary structure (SS) breaks

101   in the TMDs mediated by Glycine and Proline residues and several predicted SS breakers[32], most

102   noticeably at G317 and G329 that leads to an elongation of extracellular loop (ECL)3 and wide

103   separation between TM5 and TM6 (Figure S1). Conversely, ECL6, connecting TM11 & TM12

104   displays a lower degree of helix unraveling, likely owing to lower frequency of secondary structure

105   breaking residues that we speculate limit its conformational freedom and possibly that of TM10

106   and TM11. As shown in figure 2B, closing of the central TMD pathway is facilitated by TM4,

107   which adopts a kinked conformation with secondary structure breaks at P223 and K242, effectively

108   dividing it into 3 sub helices (TM4a-c). In conjunction with TM6 and TM12, it forms a central 3-
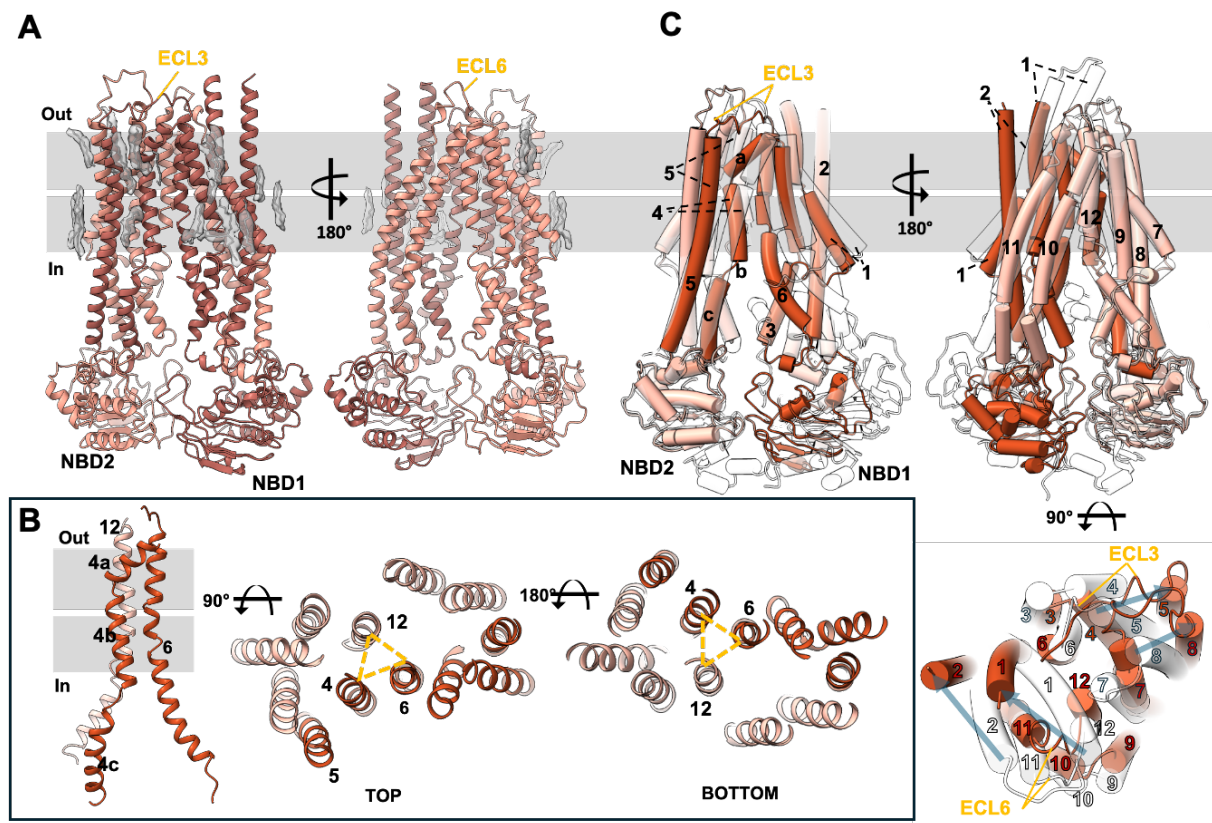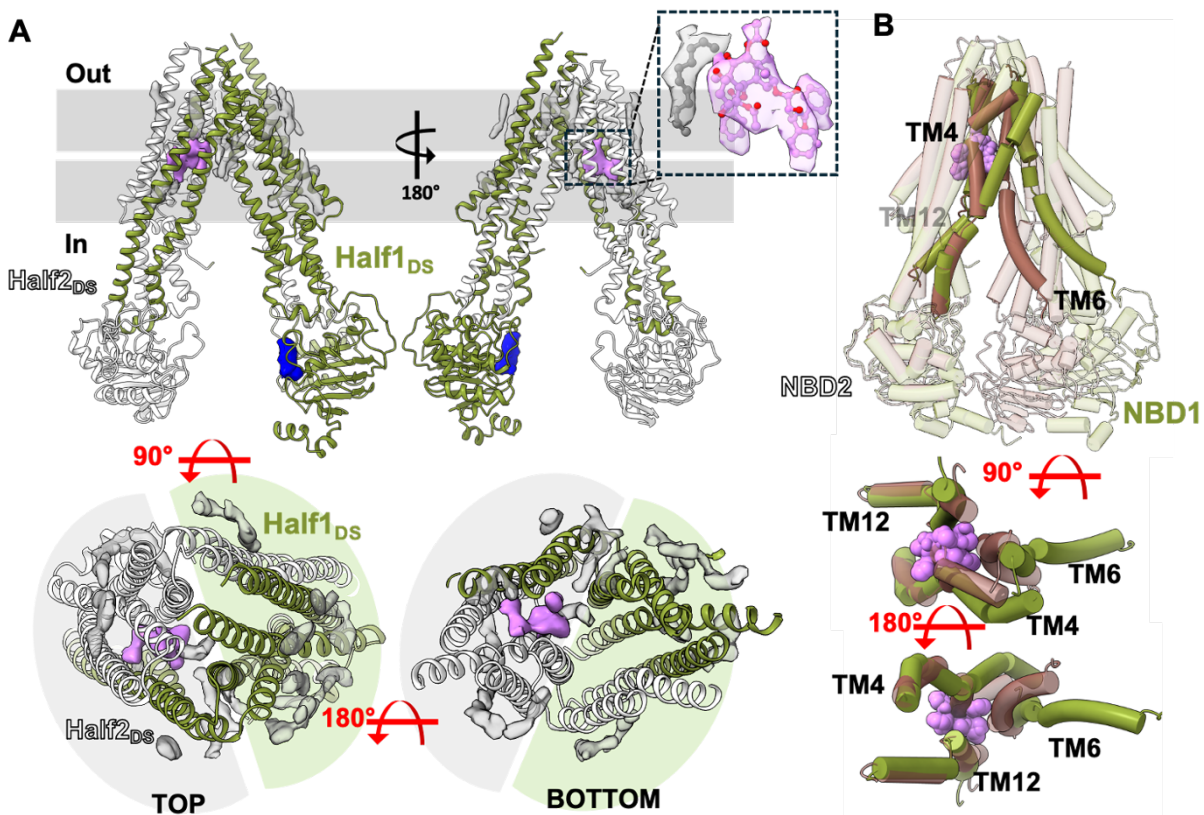

Figure 2. Structure of apo-ABCB1. A Overall structure with the two halve colored as different shades of red and density modeled as lipid acyl chains (gray sticks) shown as transparent gray surfaces. B 3TM bundle formation by TM4, TM6, and TM12. TM4 sub-helical segments. The yellow dashed triangle highlights the central 3TM bundle in top and bottom views. C Comparison of the cryo-EM structure of apo- ABCB1, colored as in A, and its alphafold predicted structure (transparent cartoon). Blue transparent arrows indicate major movements of select TMs. The gray bars represent the plasma membrane .

109   TM bundle that closes off the central cavity (Figure 1C). In contrast to TM4, TM10 adopts a

110   straight conformation, contributing further to structural asymmetry and leading to a lateral opening

111   to the lower bilayer leaflet. These features lead to an overall conformation that diverges widely

112   from canonical IF open conformations as demonstrated by a comparison to the alphafold predicted

113   structure of ABCB1 (Figure 2C). The starkest differences are between the respective positions of

114   TM1/TM2 and TM4/TM5 pairs, leading to a more splayed open asymmetric arrangement of the

115   extracellular "leaflets" and closer NBD spacing. The implications of this conformation for

116   substrate and nucleotide access are expanded upon below.

117   **Distinct Substrate and Inhibitors interactions in human ABCB1**

Figure 3 Structure of ABCB1 bound to Taxol A Overall structure with first and second halves (primary structure based) colored green and white, respectively, and distinguished from domain swapped (DS) halves. Density for Taxol and lipids is shown in pink and grey (0.01 contour threshold), respectively. Weaker density for the NBD1 nucleotide is shown in blue (0.008 contour threshold). The zoom panel shows Taxol (pink sticks) density along with associated density features modeled as a lipid acyl chain (grey sticks) as transparent pink and gray surfaces, respectively. Domain swapped halves are highlighted demarcated by grey and green semicircles B Overall comparison of apo and Taxol complexes of ABCB1 (transparent brown and green cartoons respectively) with 3TM forming helices (solid tube helices) and Taxol (pink spheres) shown

118   Previous analyses of substrate and inhibitor discrimination in human ABCB1 in the presence of

119   conformational antibody Fabs revealed that both classes could occupy a centrally located, occluded

120   TMD site with subtle differences between drug interacting residues and overall conformation[23,24].

121   Here we show that the predominant conformational states of Taxol and zosuquidar complexes with

122   ABCB1 alone are completely different. As shown in Figure 3A, Taxol bound ABCB1 adopts a

123   symmetrical IF conformation with wider NBD spacing compared to the apo state. Taxol binding,

124   however, is asymmetric, with a single molecule observed within the C-terminal half of the

125   molecule/2nd half comprising the domain swapped (DS) TMD2 (TM7-9 and TM12 from TMD2,

126   and TM4 and TM5 from TMD1) and NBD2 pair, offset from the central TMD space. Interestingly,

127   this binding site is occupied by TM4b in the apo state, which swings away to allow Taxol binding

128   (Figure 3B). This is accompanied by major rearrangements of TM5, ECL6, and TM6, breakup of

129   the 3TM bundle observed in the apo state and an outward movement of NBD1. The position of

130   NBD2 and its associated coupling helices remains largely unchanged. This links substrate binding

131   to NBD orientation through TM4, which may act as an affinity gate to add a degree of substrate

132   discrimination as expanded upon below. Density features within the hydrophobic TMD cavity are

133   consistent with the presence of lipids and/or sterols. As their specific identity and orientation are

134   impossible to ascertain from these data alone, we modeled them as unidentified acyl chains. A

135   comparison of the two domain swapped halves of Taxol bound ABCB1 reveals distinct differences

136   between residues within 5Å of the observed Taxol molecule in the C-terminal Half and its N-

137   terminal equivalent that would present a steric and electrostatic barrier to Taxol binding. (Figure

138   S2).

139   In contrast to its Taxol complex, zosuquidar bound ABCB1 adopts the same conformation

140   as seen in the antibody bound complexes, marked by a fully occluded cavity with 2 closely

141   interacting zosuquidar molecules (Figure 4A-B). Cavity occlusion is brought about by the

142   concerted kinking of TM4 and TM10, further highlighting its role in in the overall transport cycle.

143   Diffuse density for bound nucleotide is observed in NBD1. The overall structure of zosuquidar

144   bound ABCB1 shows increased positional order compared to the Taxol complex, with clearer

145   density for TMD associated lipids and NBD1 associated nucleotide. While the overwhelming

146   majority of Taxol-interacting residues are drawn from the C-terminal Half (Figure 4C), zosuquidar
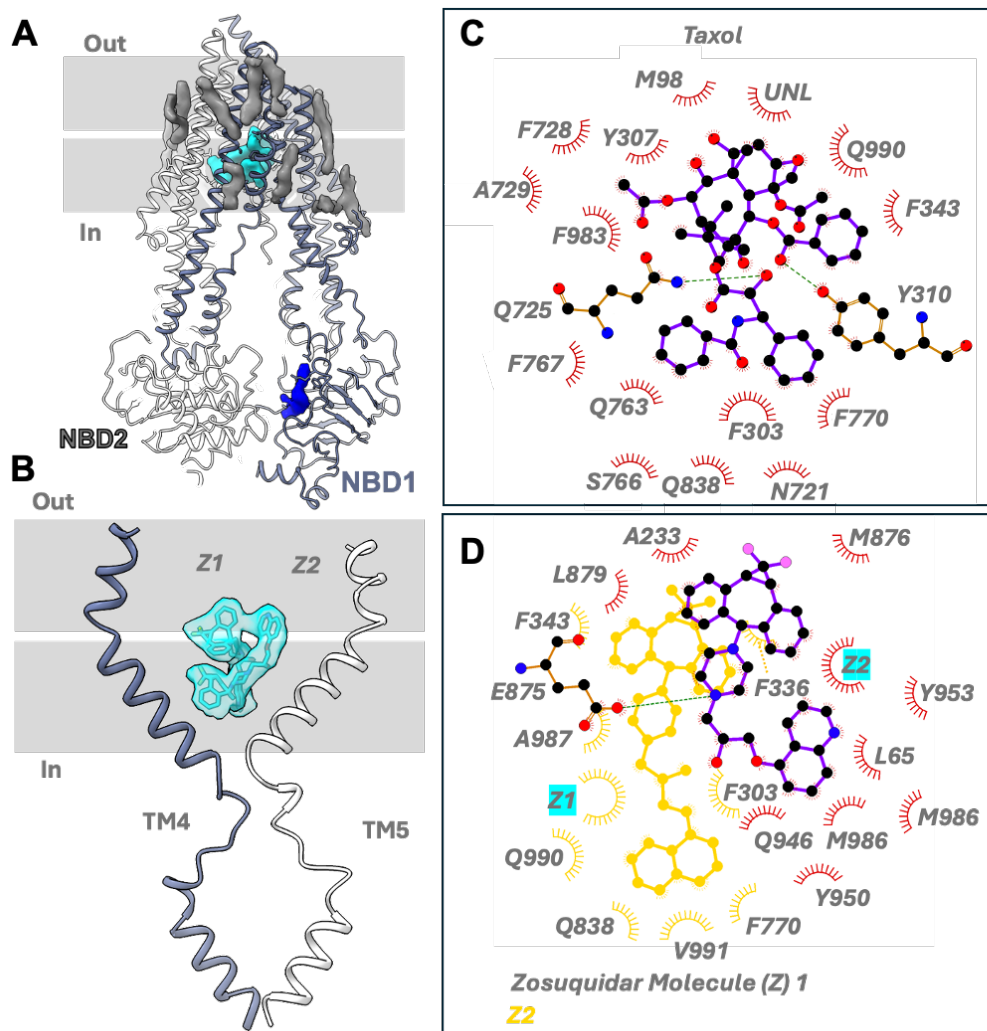
Figure 4 Comparison of Zosuquidar and Taxol binding. *A Overall structure of the ABCB1 bound to Zosuquidar. Zosuquidar and ATP density is shown (0.0175 contour) as teal and blue surfaces, respectively. B Zoomed view of the occluded TMD cavity with TM4 and TM10 shown with EM density for both Zosuquidar molecules (teal sticks, Z1 and Z2) shown as a transparent teal surface (0.017 contour). C Ligand interaction plot of ABCB1 complexed to Taxol. D Ligand interaction plot of zosuquidar bound ABCB1 with the second Zosuquidar molecule shown in yellow.*

147   interactions span both halves of the transporter (Figure 4D) and no extraneous lipid density was

148   observed in the occluded cavity.

**Structural transitions in human ABCB1 are asymmetric and dependent on TM4**
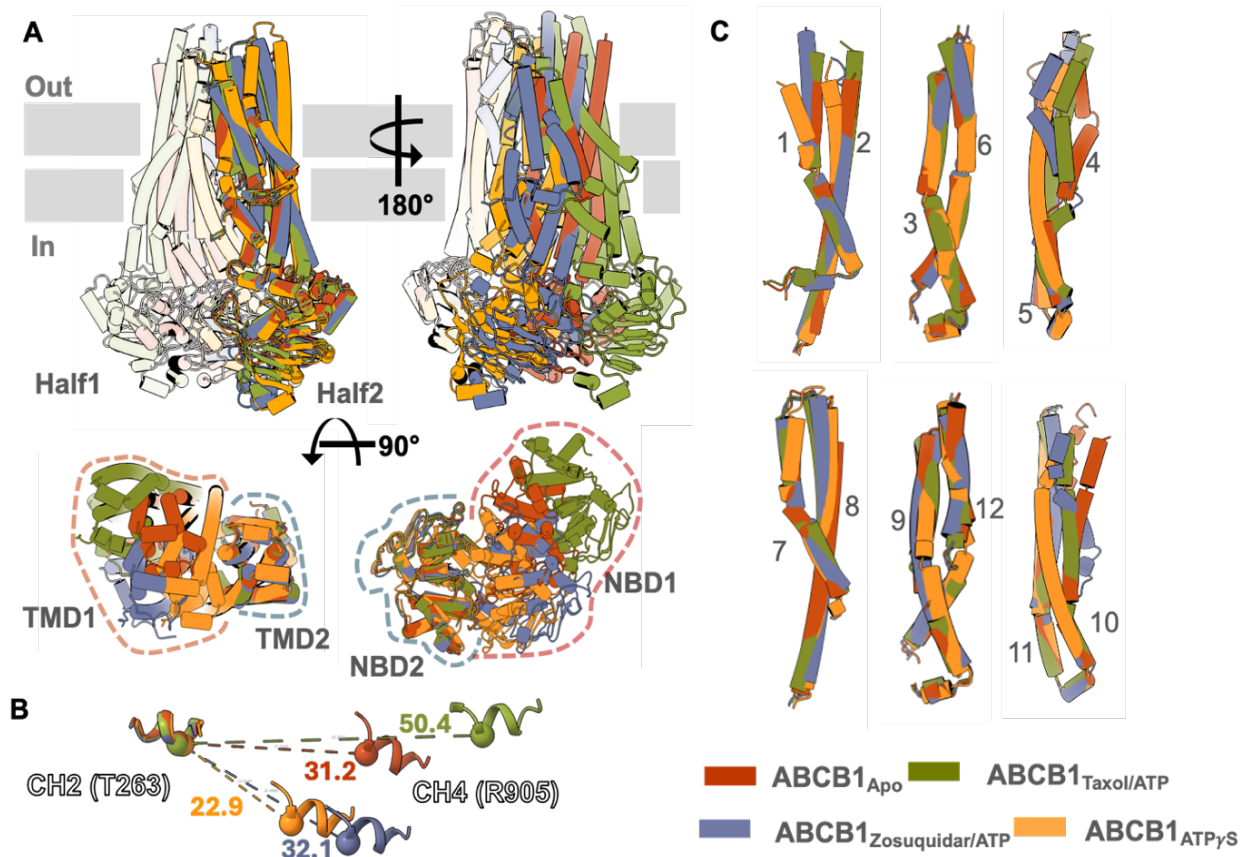
Figure 5 Structural Transitions in ABCB1. A Overlay of full transporter in all 4 conformations with Half 1 and half 2 shown as transparent surfaces (front and back views, respectively) and with individual TMDs and NBDs outlined top and bottom views, respectively. B Pairwise structural alignment of linked TM pairs expected to move together in different type II ABC exporter conformational states.

150   The four conformational states of ABCB1 presented here allow for a direct comparison of the

151   overall transitions associated with its drug transport cycle. As shown in Figure 5A, the C-terminal

152   half of the transporter remains relatively rigid in comparison to its N-terminal counterpart, with

153   significant positional changes of NBD1 associated with the different TMD conformations. Inter

154   NBD separation is similar for the apo and inhibited state with the widest separation between the

155   NBDs of the Taxol bound IF conformation and narrowest separation for the sandwiched NBD

156   dimer in the ATPγS complex as highlighted by Cα distance measurements between T263 (CH2)

157   and R905 (CH4) (Figure 5B). While the overall conformations of the 4 states diverge significantly,

158   a pairwise alignment of TM pairs 1/2, 3/6, and 4/5 (and their half 2 counterparts) shows expected

159   patterns of linked movements during conformational cycling[33] with major exceptions for TM4 and

160   TM10, and to a lesser extent, TM1 and TM2 (Figure 5C). TM4 adopts a different conformation in

161   all 4 structures, including three unique kinked conformations in the apo, substrate bound, and

162   inhibitor bound states. Similarly, TM10 adopts different conformations in all four structures, but

163   only the zosuquidar bound state displays a kinked conformation like that of TM4. The Cytoplasmic

164   halves of all TMs match very closely in all structures, revealing that the conformational changes

165   occur within the membrane environment, likely stabilized by dynamic lipid contacts, as expanded

166   upon below.

167   **Discussion**

168   Our data allow us to formulate an updated mechanism for substrate transport and its

169   inhibition in ABCB1 as shown in Figure 4B. Central to this scheme is TM4, which acts as a gating

170   helix and undergoes large-scale rearrangements in all conformations reported here. In the unbound

171   (apo) state, human ABCB1 likely exists in a conformational equilibrium between multiple IF

172   states. The IF$_{CLOSED}$ state that is dominant from our analysis is incompatible with substrate binding,

173   with TM4 involved in 3TM bundle formation to close the TMD pathway and also sterically

174   occluding the substrate binding site. As such, TM4 may play an autoinhibitory role and act as an

175   affinity filter akin to the regulatory domains of ABCC type transporters[34,35]. Substrates overcoming

176   this affinity threshold shift the conformational equilibrium towards an IF$_{OPEN}$ state with greater

177   NBD separation, concurrent opening of the 3-TM bundle, and ejection of TM4b from the substrate
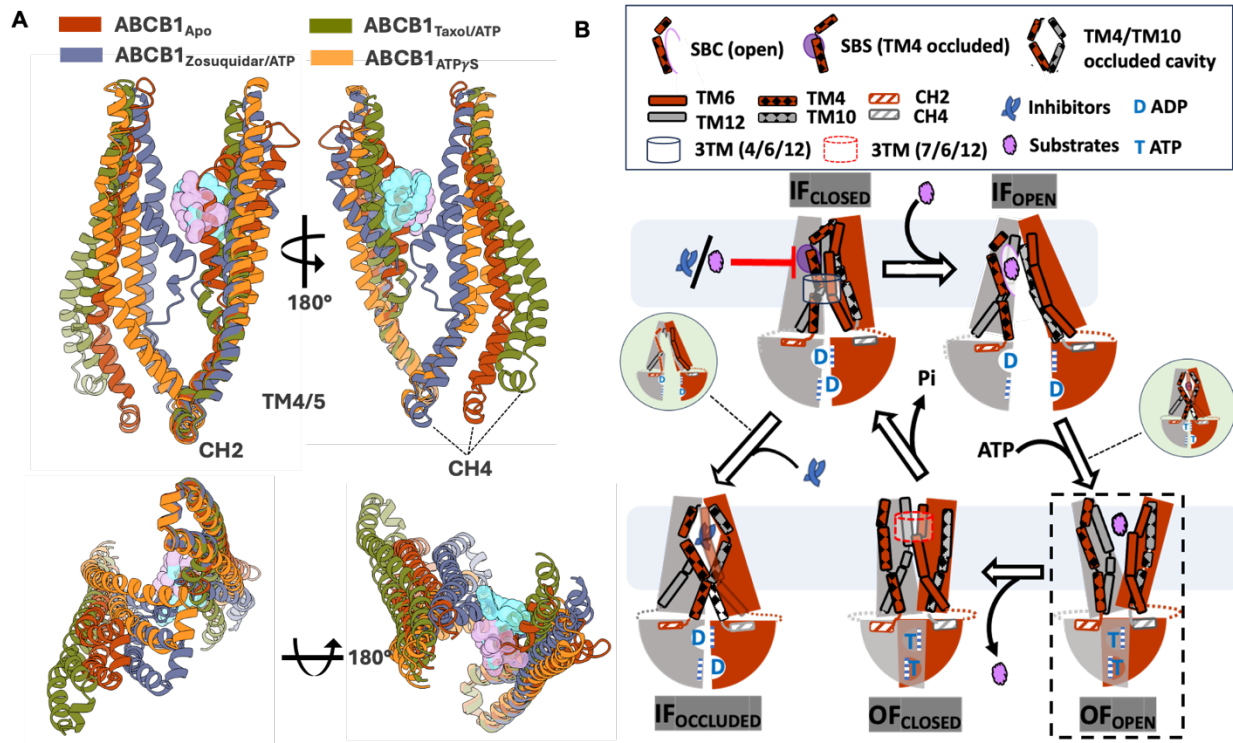
***Figure 6 Substrate and inhibitor interactions in ABCB1 A** Overlay of TM4/5 and TM10/11 of all structures reported, highlighting overall conformational changes linked to substrate (Taxol, pink) or inhibitor (zosuquidar, teal) binding and CH2 and CH4 movements **B** Schematic of working model for substrate transport and inhibition in human ABCB1. With the exception of the OF$_{OPEN}$ state (based on homologous transporters like human ABCD1[9] and Sav1866[21]). Green circles highlight potential intermediate/alternate states.*

178   binding site. Compared to the apo state, this NBD separation may be more sterically favorable for

179   ATP binding (ATP/ADP exchange), linking substrate binding to stimulation of ATPase rates. The

180   IF$_{OCCLUDED}$ state observed in the zosuquidar complex has been previously shown to be stabilized

181   by inhibitory antibodies and capable of accommodating substrates[23,24,36]. Combined with insights

182   from our current data, it likely represents a sparsely populated high-energy state prior to substrate

183   extrusion through the OF$_{OPEN}$ conformation. Inhibitors like zosuquidar, on the other hand, stabilize

184   the IF$_{OCCLUDED}$ conformation, thereby inhibiting the transport cycle. This clear difference between

185   substrates and inhibitors may be explained by their divergent ligand interactions based on our

186   observations for the Taxol and Zosuquidar complex structures described here. Asymmetry may

187   play a key role here, with inhibitors like zosuquidar able to make stabilizing interactions with both

188   domain-swapped halves of the transporter. In contrast, substrates like Taxol seen to bind within

189     $TMD2_{DS}$ may be destabilized upon contact with $TMD1_{DS}$ upon ATP binding induced NBD closure

190   and consequent TMD rearrangements, promoting a transition to the OF_{OPEN} conformation and

191   substrate extrusion. This suggests that $TMD1_{DS}$ residues that have been implicated in substrate

192   interactions through mutagenesis and cellular efflux studies but not seen to directly interact with

193   substrate here may be involved in promoting extrusion rather than stabilizing substrate binding[37-

194   42]. Upon substrate extrusion the external leaflets of ABCB1 adopt a closer arrangement in contrast

195   to OF states such as that seen in human ABCD1[9]. Interestingly, this OF_{CLOSED} state is also

196   characterized by formation of a 3TM bundle like that in the apo state, albeit involving TM6, TM7,

197   and TM12, and may similarly serve to prevent undesired substrate or lipid interactions before the

198   transporter resets upon ATP hydrolysis to its IF conformation(s).

199   Insights into TMD access and auto-inhibition of the binding site by TM4 gleaned from our

200   data fundamentally change our understanding of how human ABCB1 works. They have a number

201   of important implications for development of better ABCB1 inhibitors as well as drugs that bypass

202   its substrate transport cycle. First, the IF_{CLOSED} apo state lays the foundation for development of a

203   new class of ABCB1 inhibitors that could potentially trap it, thereby preventing substrate access

204   to the TMD. Second, the taxol complex offers unprecedented detail into a discreet substrate

205   binding site that can aid the design of more accurate computational models for studying ABCB1

206   drug interactions. Third, the zosuquidar and taxol complexes of ABCB1 define the underlying

207   binding chemistry that distinguishes substrates and inhibitors. Finally, our structural data reconcile

208   decades of mutagenesis studies and showcase the remarkable structural and functional variability

209   helix breaking elements impart to TMDs, especially in context of a lipid bilayer environment and

210   dynamic lipid interactions, that existing homology and predicted models have failed to capture.

211   Additional structures of human ABCB1 in complex with drugs with different physiochemical are

212   needed to explore the extent of binding site plasticity and potential deviations from the mechanistic

213   framework proposed above.

214

215

216

217

218

219

220

221

222

223

224

225

226

227

228

229

230

References

231   **References**

232   1   Borst, P. & Schinkel, A. H. P-glycoprotein ABCB1: a major player in drug handling by

233   mammals. *J Clin Invest* **123**, 4131-4133, doi:10.1172/JCI70430 (2013).

234   2   Hodges, L. M. *et al.* Very important pharmacogene summary: ABCB1 (MDR1, P-

235   glycoprotein).   *Pharmacogenet   Genomics   **21**,   152-161,

236   doi:10.1097/FPC.0b013e3283385a1c (2011).

237   3   Leslie, E. M., Deeley, R. G. & Cole, S. P. Multidrug resistance proteins: role of P-

238   glycoprotein, MRP1, MRP2, and BCRP (ABCG2) in tissue defense. *Toxicol Appl*

239   *Pharmacol* **204**, 216-237, doi:10.1016/j.taap.2004.10.012 (2005).

240   4   Fromm, M. F. Importance of P-glycoprotein at blood-tissue barriers. *Trends Pharmacol Sci*

241   **25**, 423-429, doi:10.1016/j.tips.2004.06.002 (2004).

242   5   Borst, P. & Elferink, R. O. Mammalian ABC transporters in health and disease. *Annu Rev*

243   *Biochem* **71**, 537-592, doi:10.1146/annurev.biochem.71.102301.093055 (2002).

244   6   Ueda, K., Cardarelli, C., Gottesman, M. M. & Pastan, I. Expression of a full-length cDNA

245   for the human "MDR1" gene confers resistance to colchicine, doxorubicin, and vinblastine.

246   *Proc Natl Acad Sci U S A* **84**, 3004-3008, doi:10.1073/pnas.84.9.3004 (1987).

247   7   Thiebaut, F. *et al.* Cellular localization of the multidrug-resistance gene product P-

248   glycoprotein in normal human tissues. *Proc Natl Acad Sci U S A* **84**, 7735-7738,

249   doi:10.1073/pnas.84.21.7735 (1987).

250   8   Darwich, A. S., Neuhoff, S., Jamei, M. & Rostami-Hodjegan, A. Interplay of metabolism

251   and transport in determining oral drug absorption and gut wall metabolism: a simulation

252   assessment using the "Advanced Dissolution, Absorption, Metabolism (ADAM)" model.

253   *Curr Drug Metab* **11**, 716-729 (2010).

254 9   Le, L. T. M., Thompson, J. R., Dang, P. X., Bhandari, J. & Alam, A. Structures of the human

255   peroxisomal fatty acid transporter ABCD1 in a lipid environment. *Commun Biol* **5**, 7,

256   doi:10.1038/s42003-021-02970-w (2022).

257 10   Fiedorczuk, K. & Chen, J. Mechanism of CFTR correction by type I folding correctors.

258   *Cell* **185**, 158-168 e111, doi:10.1016/j.cell.2021.12.009 (2022).

259 11   Bauer, F. *et al.* Synthesis and in vivo evaluation of [11C]tariquidar, a positron emission

260   tomography radiotracer based on a third-generation P-glycoprotein inhibitor. *Bioorg Med*

261   *Chem* **18**, 5489-5497, doi:10.1016/j.bmc.2010.06.057 (2010).

262 12   Leonard, G. D., Fojo, T. & Bates, S. E. The role of ABC transporters in clinical practice.

263   *Oncologist* **8**, 411-424, doi:10.1634/theoncologist.8-5-411 (2003).

264 13   Ling, V. Multidrug resistance: molecular mechanisms and clinical relevance. *Cancer*

265   *Chemother Pharmacol* **40 Suppl**, S3-8 (1997).

266 14   Robey, R. W. *et al.* Revisiting the role of ABC transporters in multidrug-resistant cancer.

267   *Nat Rev Cancer* **18**, 452-464, doi:10.1038/s41568-018-0005-8 (2018).

268 15   Schinkel, A. H., Wagenaar, E., Mol, C. A. & van Deemter, L. P-glycoprotein in the blood-

269   brain barrier of mice influences the brain penetration and pharmacological activity of many

270   drugs. *J Clin Invest* **97**, 2517-2524, doi:10.1172/JCI118699 (1996).

271 16   Xie, R., Hammarlund-Udenaes, M., de Boer, A. G. & de Lange, E. C. The role of P-

272   glycoprotein in blood-brain barrier transport of morphine: transcortical microdialysis

273   studies in mdr1a (-/-) and mdr1a (+/+) mice. *Br J Pharmacol* **128**, 563-568,

274   doi:10.1038/sj.bjp.0702804 (1999).

275 17   Storck, S. E., Hartz, A. M. S. & Pietrzik, C. U. The Blood-Brain Barrier in Alzheimer's

276   Disease. *Handb Exp Pharmacol* **273**, 247-266, doi:10.1007/164_2020_418 (2022).

18   Sita, G., Hrelia, P., Tarozzi, A. & Morroni, F. P-glycoprotein (ABCB1) and Oxidative Stress: Focus on Alzheimer's Disease. *Oxid Med Cell Longev* **2017**, 7905486, doi:10.1155/2017/7905486 (2017).

19   Loscher, W. & Potschka, H. Role of multidrug transporters in pharmacoresistance to antiepileptic drugs. *J Pharmacol Exp Ther* **301**, 7-14, doi:10.1124/jpet.301.1.7 (2002).

20   Tamaki, A., Ierano, C., Szakacs, G., Robey, R. W. & Bates, S. E. The controversial role of ABC transporters in clinical oncology. *Essays Biochem* **50**, 209-232, doi:10.1042/bse0500209 (2011).

21   Dawson, R. J. & Locher, K. P. Structure of the multidrug ABC transporter Sav1866 from Staphylococcus aureus in complex with AMP-PNP. *FEBS Lett* **581**, 935-938, doi:10.1016/j.febslet.2007.01.073 (2007).

22   Dawson, R. J. & Locher, K. P. Structure of a bacterial multidrug ABC transporter. *Nature* **443**, 180-185, doi:10.1038/nature05155 (2006).

23   Alam, A., Kowal, J., Broude, E., Roninson, I. & Locher, K. P. Structural insight into substrate and inhibitor discrimination by human P-glycoprotein. *Science* **363**, 753-756, doi:10.1126/science.aav7102 (2019).

24   Nosol, K. *et al.* Cryo-EM structures reveal distinct mechanisms of inhibition of the human multidrug transporter ABCB1. *Proc Natl Acad Sci U S A* **117**, 26245-26253, doi:10.1073/pnas.2010264117 (2020).

25   Clay, A. T., Lu, P. & Sharom, F. J. Interaction of the P-Glycoprotein Multidrug Transporter with Sterols. *Biochemistry* **54**, 6586-6597, doi:10.1021/acs.biochem.5b00904 (2015).

298   26   Hegedus, C., Telbisz, A., Hegedus, T., Sarkadi, B. & Ozvegy-Laczka, C. Lipid regulation

299   of the ABCB1 and ABCG2 multidrug transporters. *Adv Cancer Res* **125**, 97-137,

300   doi:10.1016/bs.acr.2014.10.004 (2015).

301   27   Loo, T. W. & Clarke, D. M. P-glycoprotein ATPase activity requires lipids to activate a

302   switch at the first transmission interface. *Biochem Biophys Res Commun* **472**, 379-383,

303   doi:10.1016/j.bbrc.2016.02.124 (2016).

304   28   Szewczyk, P. *et al.* Snapshots of ligand entry, malleable binding and induced helical

305   movement in P-glycoprotein. *Acta Crystallogr D Biol Crystallogr* **71**, 732-741,

306   doi:10.1107/S1399004715000978 (2015).

307   29   Yu, Q. *et al.* Structures of ABCG2 under turnover conditions reveal a key step in the drug

308   transport mechanism. *Nat Commun* **12**, 4376, doi:10.1038/s41467-021-24651-2 (2021).

309   30   Kim, Y. & Chen, J. Molecular structure of human P-glycoprotein in the ATP-bound,

310   outward-facing conformation. *Science* **359**, 915-919, doi:10.1126/science.aar7389 (2018).

311   31   Aller, S. G. *et al.* Structure of P-glycoprotein reveals a molecular basis for poly-specific

312   drug binding. *Science* **323**, 1718-1722, doi:10.1126/science.1168750 (2009).

313   32   Imai, K. & Mitaku, S. Mechanisms of secondary structure breakers in soluble proteins.

314   *Biophysics (Nagoya-shi)* **1**, 55-65, doi:10.2142/biophysics.1.55 (2005).

315   33   Lee, J. Y., Yang, J. G., Zhitnitsky, D., Lewinson, O. & Rees, D. C. Structural basis for heavy

316   metal detoxification by an Atm1-type ABC exporter. *Science* **343**, 1133-1136,

317   doi:10.1126/science.1246489 (2014).

318   34   Mao, Y. X. *et al.* Transport mechanism of human bilirubin transporter ABCC2 tuned by the

319   inter-module regulatory domain. *Nat Commun* **15**, 1061, doi:10.1038/s41467-024-45337-

320   5 (2024).

321   35   Khandelwal, N. K. & Tomasiak, T. M. Structural basis for autoinhibition by the
322   dephosphorylated regulatory domain of Ycf1. *Nat Commun* **15**, 2389, doi:10.1038/s41467-
323   024-46722-w (2024).

324   36   Alam, A. *et al.* Structure of a zosuquidar and UIC2-bound human-mouse chimeric ABCB1.
325   *Proc Natl Acad Sci U S A* **115**, E1973-E1982, doi:10.1073/pnas.1717044115 (2018).

326   37   Loo, T. W. & Clarke, D. M. Mapping the Binding Site of the Inhibitor Tariquidar That
327   Stabilizes the First Transmembrane Domain of P-glycoprotein. *J Biol Chem* **290**, 29389-
328   29401, doi:10.1074/jbc.M115.695171 (2015).

329   38   Loo, T. W. & Clarke, D. M. Mutational analysis of ABC proteins. *Arch Biochem Biophys*
330   **476**, 51-64, doi:10.1016/j.abb.2008.02.025 (2008).

331   39   Loo, T. W. & Clarke, D. M. Mutational analysis of human P-glycoprotein. *Methods*
332   *Enzymol* **292**, 480-492 (1998).

333   40   Chufan, E. E., Kapoor, K. & Ambudkar, S. V. Drug-protein hydrogen bonds govern the
334   inhibition of the ATP hydrolysis of the multidrug transporter P-glycoprotein. *Biochem*
335   *Pharmacol* **101**, 40-53, doi:10.1016/j.bcp.2015.12.007 (2016).

336   41   Chufan, E. E. *et al.* Multiple transport-active binding sites are available for a single
337   substrate   on   human   P-glycoprotein   (ABCB1).   *PLoS   One*   **8**,   e82463,
338   doi:10.1371/journal.pone.0082463 (2013).

339   42   Nasim, F. *et al.* Active transport of rhodamine 123 by the human multidrug transporter P-
340   glycoprotein involves two independent outer gates. *Pharmacol Res Perspect* **8**, e00572,
341   doi:10.1002/prp2.572 (2020).

342

343

344   **Methods**

345   **Cell Culture, Protein expression and purification**

346   The expression and purification of wild-type human ABCB1 were conducted largely as previously

347   described[23,24,36]. First, an ABCB1 stable cell line with a C-terminal eYFP-Rho1D4 tag and a

348   3C/precision protease site between the protein and tag was generated using the FIp-In TREX

349   system (Thermo Fisher Scientific) for tetracycline-inducible expression. These ABCB1 stable

350   cells were grown in DMEM media supplemented with 10% fetal bovine serum (FBS), penicillin-

351   streptomycin, and antimycotic antibiotics at 37 °C in a 5% CO2 incubator until they reached over

352   70% confluency, which typically took about 72-96 hours. Next, the media was replaced with

353   DMEM supplemented with 2% FBS and 0.6 µg/ml tetracycline, and the cells were allowed to

354   express the protein for 72 hours at 37 °C in a 5% CO2 incubator. These cells were subsequently

355   washed with PBS before being harvested by centrifugation at 3000 r.c.f for 3 minutes at 4 °C, and

356   flash-frozen in liquid nitrogen for storage at -80 °C.

357   All protein purification steps were carried out at 4°C or on ice. Cell pellets were thawed

358   and resuspended in eight volumes of lysis buffer per gram of pellet (25 mM HEPES pH 7.5, 150

359   mM NaCl, 20% glycerol, 0.5 mM PMSF, 2 µg/ml trypsin inhibitor, and one complete mini tablet

360   per 50 ml). After dounce homogenizing, the cell lysate incubated with a 0.5%/0.1% mixture of n-

361   dodecyl-β-D-maltopyranoside (DDM) and cholesteryl hemisuccinate (CHS) for 2 hours, and then

362   centrifuged at 48000 r.c.f for 30 minutes. The supernatant was applied to Cyanogen bromide-

363   activated Sepharose 4b beads (Cytiva) coupled to rho1D4 antibody (University of British

364   Columbia) resin for binding over 3 hours. The resin was washed four times with 10 column

365   volumes (CV) of wash buffer (25 mM HEPES pH 7.5, 150 mM NaCl, 20% glycerol, and

366   0.02%/0.004% DDM/CHS) followed by protein elution by addition of Wash Buffer supplemented

367 either with 0.25 mg^{-1}ml^{-1} 1D4 peptide (GenScript) or a 1:10 w:w ratio of 3C protease for on-

368 column cleavage and incubated overnight at 4 °C on a roller for tag cleavage. 3C protease was

369 removed by incubation with Ni-NTA beads.

370

371 **Lipid reconstitution of ABCB1**

372 Expression and purification of MSP1D1 (Addgene) and Saposin A (Salipro) was carried out as

373 described[43,44] except that the final purification and storage buffer contained 25 mM HEPES pH

374 7.5, 150 mM NaCl. Brain Polar Extract lipids (BPL, Avanti) and cholesterol (Chol, Sigma) were

375 mixed at an 80:20 w:w ratio and dried using a rotary evaporator (Bucchi), resuspended in diethyl

376 ether, dried again, and finally resuspended in HEPES buffer (25 mM HEPES pH 7.5, 150 mM

377 NaCl). Nanodisc reconstitution followed our published protocols[9,45]. Briefly, The BPL/Chol

378 mixture was solubilized in storage buffer supplemented with a 0.2%/0.04% solution of DDM/CHS

379 and homogenized using water bath sonication, with three cycles of 2 minutes on and 2 minutes

380 off. 3C cleaved or ID4 peptide eluted ABCB1 was mixed with MSP1D1 and solubilized lipids a

381 molar ratio of 1:10:350 for ABCB1:MSP1D1:BPL/Chol and the mixture diluted to reduce the final

382 glycerol concentration to less than 4% (v:v). After 1-hour incubation at 4 °C on a roller, detergent

383 was removed by addition of 0.8 grams ml^{-1} reaction buffer of Bio-Beads SM-2 (Biorad) prewashed

384 in storage buffer and incubation on a roller for 2 hours at room temperature (RT). The supernatant

385 was removed from the biobeads and concentrated using a 100kDA molecular weight cut off

386 (M.W.C.O) centrifugal filter. Saposin A reconstituted ABCB1 was prepared similarly except that

387 a 1:15:400 molar ratio of ABCB1:Saposin A:BPL/Chol was used. Protein concentration was

388 measured by densitometry analysis of SDS-PAGE bands using detergent purified ABCB1 of

389 known concentrations as standards.

390   ABCB1 proteoliposomes were prepared as described[46] with minor modifications. Briefly, the

391   BPL/Chol lipid mixture (80:20 wt:wt ratio) was first reconstituted in buffer comprising 150mM

392   NaCl and 25mM Hepes pH 7.5 at a concentration of $20mg^{-1}ml^{-1}$. Empty liposomes were prepared

393   through extrusion using a 0.2 μm filter. Pre-formed liposomes and detergent-purified ABCB1 were

394   supplemented with at 0.3 % and 0.14 % (v:v) of Triton X-100, respectively, mixed, and incubated

395   at RT for 30 minutes. Detergent removal was done in five successive incubation steps using each

396   using fresh 50 mg Bio-beads SM-2 per ml reaction mix. The incubation steps were carried out with

397   gentle agitation for 30 mins at RT, 60 mins at 4°C, overnight at 4 °C, followed by two 60-minute

398   incubations at 4 °C. Liposomes were pelleted by ultracentrifugation at 80,000 r.p.m using a TLA-

399   100 rotor (Beckmann Coulter), the supernatant discarded and resuspended in an equivalent volume

400   of reconstitution buffer at $0.5\text{-}1\ mg^{-1}ml^{-1}$.

401

402   **ATPase Assays**

403   ATPase measurements were based on a molybdate-based calorimetric assay measuring release of

404   inorganic phosphate (Pi) [47] as described[9,45]. Stocks of zosuquidar (Tocris) and taxol (PhytoLab)

405   were prepared in 100% Dimethyl sulfoxide DMSO. ATPase measurements were performed by

406   incubating $0.02\text{-}0.1\ mg^{-1}ml^{-1}$ ABCB1 with 2mM ATP, 10mM $MgCl_2$ with varying concentrations

407   of zosuquidar or taxol at 37°C. Statistical analyses and linear regression were done in GraphPad

408   Prism 9. All assays were replicates of three independent experiments.

409

410   **Native-Mass spectrometry**

411   Wild-type ABCB1 was purified and reconstituted into nanoparticles as described in the above

412   sections. The detergent sample and the reconstituted ABCB1 samples were buffer exchanged into

413   200 mM ammonium acetate (99.999% Trace Metals Basis, Sigma Aldrich) containing 0.02%

414   DDM/0.004% CHS (only 200 mM ammonium acetate for nanoparticle sample) using 40k zeba

415   spin desalting column and further purified by injecting into an Agilent 1260 Infinity II LC system

416   (Agilent Technologies) using pre-equilbrated TSKgel G4000SWxl column (TOSOH biosciences)

417   Samples were diluted to 500 nM and ionized via nano-electrospray ionization using gold coated

418   borosilicate capillaries (prepared in-house) and analyzed on a Q Exactive Ultra High Mass Range

419   orbitrap mass spectrometer (Thermo Fisher Scientific)[48,49]. The instrument was operated in Direct

420   Mass mode, enabling orbitrap-based charge detection mass spectrometry measurements of

421   individual intact lipoprotein nanoparticle ions[50,51]. Briefly, the instrument was operated with the

422   Ion Target set to "high m/z" and the Detector Optimization set to "low m/z." The in-source

423   trapping and higher-energy collisional dissociation cell were operated at 1-10 V. All measurements

424   were acquired at a resolution setting of 200,000 (FWHM at m/z 400) with a trapping gas pressure

425   setting of 1. All data processing was performed using STORIBoard (Proteinaceous Inc.). Ions were

426   filtered based on ion lifetime and signal-to-noise, and ion charge states were assigned using the

427   "Voting v3" charge assignment algorithm[51]. Ion filtering and charge assignment parameters are

428   summarized in Table S1. Charge assignment was calibrated using carbonic anhydrase, alcohol

429   dehydrogenase, pyruvate kinase, beta-galactosidase, and GroEl. All samples were acquired for 10-

430   20 minutes, and the reported measurements are representative of ~10,000 ions.

431

432   **Cryo EM Sample Preparation & Data collection**

433   For Grid preparation ABCB1-eYFP reconstituted in Saposin A Nanoparticles (SapNPs)

434   were incubated antiGFP nanobody (Addgene) coupled Sepharose 4B resin prepared in house for

435   2 hrs at 4°C, washed with 3 x 10CV of reconstitution buffer, followed on-column cleavage by in

436   3CV reconstitution buffer supplemented with 3C protease to recover ABCB1 SapNPs. Samples

437   were subsequently concentrated using a 100 MWCO centrifugal filter and further purified by Size

438   exclusion chromatography (SEC) on an Agilent 1260 Infinity II LC system (Agilent Technologies)

439   using a TSKgel G4000SWxl column (TOSOH biosciences) pre-equilibrated with reconstitution

440   buffer at 4 °C and peak fractions pooled and concentrated to 0.5-1 $mg^{-1}ml^{-1}$ for grid preparation .

441   Where needed zosuquidar and taxol were added to pooled fractions at 10 µM final concentration

442   with or without ATP/Mg^{2+} (5mM each) and incubated for 10 minutes at RT before concentration.

443   4 µL of sample was applied to the glow discharged (60 s, 15 mA) Quantifoil R1.2/1.3 Cu grids

444   using Vitrobot Mark IV with 4 s blot time and 0 blot force under >90 % humidity at 4 °C and

445   plunge frozen in liquid ethane. All grids were clipped and stored in liquid nitrogen.

446   All the Cryo EM data were collected on a 300 kV Titan Krios electron microscope

447   equipped with a Biocontinuum K3 Direct Electron Detector with 20 eV GIF energy filter, 50 eV

448   condenser C2 and 100 µm objective apertures. Automated data collection was carried out using

449   the EPU 2.8.0.1256REL software package (Thermo Fisher Scientific) at a magnification of

450   130,000× in Counted Super Resolution mode corresponding to a calibrated pixel size of 0.664 Å

451   with defocus range set from −0.5 µm to −2.5 µm. Three shots were taken per hole. Image stacks

452   comprising 40 frames were recorded for 60 s at an estimated dose rate of $1e-/Å^2/frame$.

453   **Data processing, model building, and refinement**

454   Data processing was done in Relion[52-54]. In brief, image stacks were motion corrected using

455   Relion's internal MotionCor2 implementation, followed by CTF estimation using CTFFIND4[55].

456   All resolution estimates were based on the gold standard 0.143 cutoff criterion[53]. Data collection

457   and processing parameters are provided in Table S2 along with model building and refinement

458   statistics. Data processing flow charts are shown in Figure S3. EM density around individual

459　domains/TMs and Local resolution-colored maps are shown in Figure S5 and Figure S6,

460　respectively.

461　　For ABCB1-apo, an initial dataset comprising 5974 micrographs was used for reference

462　free automated particle picking (Laplacian-of-Gaussian algorithm) within Relion. 2167202

463　particles were extracted at a 3x binned pixel size of 1.992 Å and subjected to several rounds of 2D

464　classification, followed by Ab-initio model building using within Relion. This initial model was

465　used for subsequent 3D classification (number of classes (N)=5) and a single predominant class

466　comprising 662694 was refined to 5.1 Å followed by another round of 3D classification (N=5) and

467　3D refinement, re-extraction at a 1.5X binned pixel size of 0.996 Å, and particle polishing to yield

468　a 4.1 Å map. A second set of 6321903 particles from 13327 micrographs was picked using Topaz

469　(default model) and processed similarly except that a refined 3D class from the first set was used

470　as a reference. A refined 3D at 4.0 Å resolution and comprising 660276 particles was obtained.

471　Particles from the final refined classes from both sets were combined, followed by additional

472　rounds of 3D refinement and postprocessing to yield a 3.8 Å map.

473　　For the ABCB1$_{Taxol/ATP}$ complex, 15494460 particles from 33055 micrographs were

474　autopicked using Topaz and extracted at a 3x binned pixel size of 1.992 Å. After one round of 2D

475　Classification, 6254156 particles were used for 3D classification (N=5) with a low pass filtered

476　ABCB1-apo map as a reference. The single highest resolution class revealed an IF conformation

477　and was subjected to iterative 3D refinement and particle polishing, followed by subtraction of the

478　SapNP. After 3D classification (N=5), 154538 particles from the highest resolution were reverted

479　to their original non-subtracted images and refined to 3.9 Å.

480　　For the ABCB1$_{Taxol}$ complex, 5725 micrographs were used to pick 2547172 particles by

481　Topaz and extracted at a 3x binned pixel size of 1.992 Å. After 2D classification, 1270596 particles

482 were used for 3D classification (N=3) using the ABCB1$_{apo}$ map as a reference. 486111 particles

483 from the best class were subjected to another round of 3D classification. The single highest

484 resolution class comprised 133895 particles and was refined to 4.7 Å.

485   For the ABCB1$_{Zosuquidar}$ complex, 2182930 particles were automatically picked by Topaz

486 from 7281 micrographs. After two rounds of 2D classification, 943398 particles entered 3D

487 classification (N=5) with a low-pass filtered ABCB1$_{apo}$ map used as a reference The single, highest

488 resolution class comprising 373279 particles was subjected to re-extraction at a 1.5X binned pixel

489 size of 0.996 Å and signal subtraction to remove delocalized bulk lipid density and refined to 3.6

490 Å resolution.

491   For the ABCB1$_{Zosuquidar/ATP}$ complex, 10710935 particles from 12897 micrographs were

492 picked using topaz. 2468729 particles were chosen for 3D classification (N=5) using the map of

493 the zosuquidar complex without ATP as a reference. A single highest resolution class comprising

494 733688 particles was subjected to iterative rounds of 3D classification and particle polishing within

495 Relion to yield a final refined map at 3.6 Å resolution.

496   Fort the ABCB1$_{ATP\gamma S}$ sample, 7689616 particles from 12165 micrographs were

497 automatically picked using Topaz. After several rounds of 2D classification, 1732065 particles

498 were subjected to 3D classification (N=5)using a low pass filtered ABCAB1$_{Apo}$ map as a reference.

499 A single OF classes comprising 400787 particles was subjected to another round of 3D

500 classification (N=5). 180,163 Particles from two similar and roughly equally populated OF classes

501 were combined, re-extracted at a 1.5X binned pixel size of 0.996 Å and refined to 3.75 Å. A second

502 dataset of 6204620 particles from 9318 micrographs was processed similarly to yield a final

503 refined class at 3.5 Å comprising 260172 particles. Particles from the final class from both datasets

504   were combined and subjected to another round of 3D classification (N=5) and the highest

505   resolution class comprising 136896 particles was refined to 3.4 Å.

506   Final EM maps were used for model building in COOT 0.9.6 EL[56]. De novo model building

507   was guided by the predicted structure of ABCB1 from AlphaFold2[57] for the apo and taxol

508   complexes. For the zosuquidar complexes, model building was guided initially by the structure of

509   ABCB1 bound to the MRK16 fab (PDBID 7A6F). For the ATPγS complexed ABCB1, the

510   structure of ATP bound ABCB1-EQ (PDBID: 6C0V) was used as an initial model before minor

511   adjustments and refinement. Non-proteinaceous continuous density features attributed to lipids or

512   sterols were modeled as Acyl-chains. The structures were refined with secondary structure and

513   geometry restrains in COOT 0.9.6 and PHENIX[58]. Where NBD density was too weak for denovo

514   model building, docked NBDs from higher resolution structures reported here were used and

515   minimally refined. The final models for ABCB1$_{apo}$ comprised residues 33-81, 106-606, 694-1230,

516   for ABCB1$_{Taxol/ATP}$ comprised residues 30-87, 100-630, 689-1257, for ABCB1$_{Zosuquidar/ATP}$

517   comprised residues 30-90, 104-630, 691-1272, and for ABCB1$_{ATP\gamma S}$ comprised residues 35-80,

518   105-630, 692-1276. Map and Structure visualization was performed in UCSF Chimera[59] and

519   ChimeraX[60].

520

521   **References (Methods)**

522

523   43   Ritchie, T. K. *et al.* Chapter 11 - Reconstitution of membrane proteins in phospholipid

524   bilayer nanodiscs. *Methods Enzymol* **464**, 211-231, doi:10.1016/S0076-6879(09)64011-8

525   (2009).

526   44   Frauenfeld, J. *et al.* A saposin-lipoprotein nanoparticle system for membrane proteins. *Nat*

527   *Methods* **13**, 345-351, doi:10.1038/nmeth.3801 (2016).

528   45   Le, L. T. M. *et al.* Cryo-EM structures of human ABCA7 provide insights into its

529   phospholipid   translocation   mechanisms.   *EMBO   J*   **42**,   e111065,

530   doi:10.15252/embj.2022111065 (2023).

531   46   Geertsma, E. R., Nik Mahmood, N. A., Schuurman-Wolters, G. K. & Poolman, B.

532   Membrane reconstitution of ABC transporters and assays of translocator function. *Nat*

533   *Protoc* **3**, 256-266, doi:10.1038/nprot.2007.519 (2008).

534   47   Chifflet, S., Torriglia, A., Chiesa, R. & Tolosa, S. A method for the determination of

535   inorganic phosphate in the presence of labile organic phosphate and high concentrations of

536   protein: application to lens ATPases. *Anal Biochem* **168**, 1-4 (1988).

537   48   Wilm, M. & Mann, M. Analytical properties of the nanoelectrospray ion source. *Anal Chem*

538   **68**, 1-8, doi:10.1021/ac9509519 (1996).

539   49   Fort, K. L. *et al.* Expanding the structural analysis capabilities on an Orbitrap-based mass

540   spectrometer   for   large   macromolecular   complexes.   *Analyst*   **143**,   100-105,

541   doi:10.1039/c7an01629h (2017).

542   50   Worner, T. P. *et al.* Resolving heterogeneous macromolecular assemblies by Orbitrap-based

543   single-particle   charge   detection   mass   spectrometry.   *Nat   Methods*   **17**,   395-398,

544   doi:10.1038/s41592-020-0770-7 (2020).

545   51   Kafader, J. O. *et al.* STORI Plots Enable Accurate Tracking of Individual Ion Signals. *J Am*

546   *Soc Mass Spectrom* **30**, 2200-2203, doi:10.1007/s13361-019-02309-0 (2019).

547   52   Zivanov, J. *et al.* A Bayesian approach to single-particle electron cryo-tomography in

548   RELION-4.0. *Elife* **11**, doi:10.7554/eLife.83724 (2022).

549 53 Scheres, S. H. RELION: implementation of a Bayesian approach to cryo-EM structure

550 determination. *J Struct Biol* **180**, 519-530, doi:10.1016/j.jsb.2012.09.006 (2012).

551 54 Kimanius, D. *et al.* Data-driven regularization lowers the size barrier of cryo-EM structure

552 determination. *Nat Methods*, doi:10.1038/s41592-024-02304-8 (2024).

553 55 Rohou, A. & Grigorieff, N. CTFFIND4: Fast and accurate defocus estimation from electron

554 micrographs. *J Struct Biol* **192**, 216-221, doi:10.1016/j.jsb.2015.08.008 (2015).

555 56 Brown, A. *et al.* Tools for macromolecular model building and refinement into electron

556 cryo-microscopy reconstructions. *Acta Crystallogr D Biol Crystallogr* **71**, 136-153,

557 doi:10.1107/S1399004714021683 (2015).

558 57 Jumper, J. *et al.* Highly accurate protein structure prediction with AlphaFold. *Nature* **596**,

559 583-589, doi:10.1038/s41586-021-03819-2 (2021).

560 58 Adams, P. D. *et al.* PHENIX: a comprehensive Python-based system for macromolecular

561 structure solution. *Acta Crystallogr D Biol Crystallogr* **66**, 213-221,

562 doi:10.1107/S0907444909052925 (2010).

563 59 Pettersen, E. F. *et al.* UCSF Chimera--a visualization system for exploratory research and

564 analysis. *J Comput Chem* **25**, 1605-1612, doi:10.1002/jcc.20084 (2004).

565 60 Pettersen, E. F. *et al.* UCSF ChimeraX: Structure visualization for researchers, educators,

566 and developers. *Protein Sci* **30**, 70-82, doi:10.1002/pro.3943 (2021).

567

568 **Acknowledgments**

Author Contributions

AA conceived the research. DK performed all experiments with contributions from LTML, AA, and PXD. AA and DK performed all cryo-EM Data processing, model building, and refinement. V.V.G performed the nMS data collection analysis simulations. AA and DK wrote the manuscript with contributions from all other authors.

Competing Financial Interests

The authors declare no competing financial Interests.

Data and materials availability:

Requests for materials should be addressed to Amer Alam. The cryo-EM Maps have been deposited at the Electron Microscopy Databank (EMDB) under accession codes EMD-45854 (ABCB1$_{apo}$), EMD-45904 (ABCB1$_{Taxol/ATP}$), EMD-45903 (ABCB1$_{Zosuquidar/ATP}$), and EMD-45906 (ABCB1$_{ATP\gamma S}$) and the associated atomic coordinates have been deposited at the Protein Data bank (PDB) under accession codes 9CR8, 9CTF, 9CTC, and 9CTG, respectively. Maps for ABCB1$_{Taxol}$ and ABCB1$_{Zosuquidar}$ have been deposited at the EMDB with accession codes MD-45931 and EMD-45932, respectively.

Additional Information

Supplementary Information is available for this manuscript.

595 **Supplementary Data**

596 **Tables S1-S2**

597 **Figures S1-S6**

598

599

600

601

602

603

604

605

606

607

608

609

610

611

612

613

614

615

616

617

Table S1: Ion filtering and charge assignment parameters

Ion Filtering	
R^2 Threshold	0.996
Duration threshold	0.42
Minimum Time of Death	0.2
Maximum Time of Birth	0.1
Signal-To-Noise Threshold	3
Charge Assignment (Voting v3)	
Bin Size (ppm)	5
Minimum Ions in Bin	1
Number of Charge Neighbors	2
Number of Isotope Neighbors	5

618

619

620

621

622

623

624

625

626

627

628

629

630

631

632

633

634
635

636 **Table S2 Cryo-EM data collection, refinement and validation statistics of human ABCB1**

Data collection and processing	ABCB1$_{apo}$	ABCB1 Taxol/ATP	ABCB1 Zosuquidar/ATP	ABCB1 ATPγS	ABCB1 Zosuquidar	ABCB1 Taxol
Microscope	FEI Titan Krios					
Camera	Gatan Biocontinuum K3					
Magnification	130kx					
Voltage (kV)	300					
Electron exposure (e^{-}/Å^2)	45-50					
Defocus range (μm)	-0.5 to -2.5					
Pixel size (Å)	0.664					
Energy filter (eV)	20					
Micrographs (#)				9318	7281	
Symmetry imposed	C1					
Particles in final Class	660276	154538	733688	136896	373279	133895
Map resolution (Å) (FSC 0.143)	3.8	3.9	3.6	3.4	3.6	4.7
Map sharpening B factor (Å^2)	-197.74	-168.435	-223.113	-137.7	-148.229	-240.975
Local Resolution Range (Å^2)	3.7-4.9	3.8-5.9	3.5-4.5	3.4-5.0		
Refinement	ABCB1$_{apo}$	ABCB1 Taxol/ATP	ABCB1 Zosuquidar/ATP	ABCB1$_{ATP\gamma S}$		
Model composition Non-hydrogen atoms Protein residues Ligands	8664 1087 15	9398 1158 24	9525 1170 25	9128 1157 13		
B factors (Å^2) Protein Ligand	65.21 41.21	128.74 100.83	79.80 60.54	70.65 62.68		
R.m.s. deviations Bond lengths (Å) Bond angles (°)	0.003 0.489	0.002 0.483	0.003 0.516	0.004 0.579		
Validation MolProbity score Clashscore Poor rotamers (%)	1.84 7.50 0.22	1.62 9.52 0.52	1.73 6.72 0.31	1.59 7.68 0.11		
Ramachandran plot Favored (%) Allowed (%) Disallowed (%)	93.52 6.48 0.0	97.40 2.52 0.09	94.85 4.81 0.34	97.05 2.95 0		

637

638

639 **Figure S1**

640

Figure S1. Secondary structure (SS) breaks in apo ABCB1 Gly and Pro residues colored teal
and blue, respectively, and predicted SS breaks shown as spheres. An ECL3 and ECL6 sequence
alignment is also shown with residues colored similarly and predicted SS breaking residues
underlined. TM4/5 and TM10/11 pairs are colored red. Acyl chains for prospective lipid/sterol
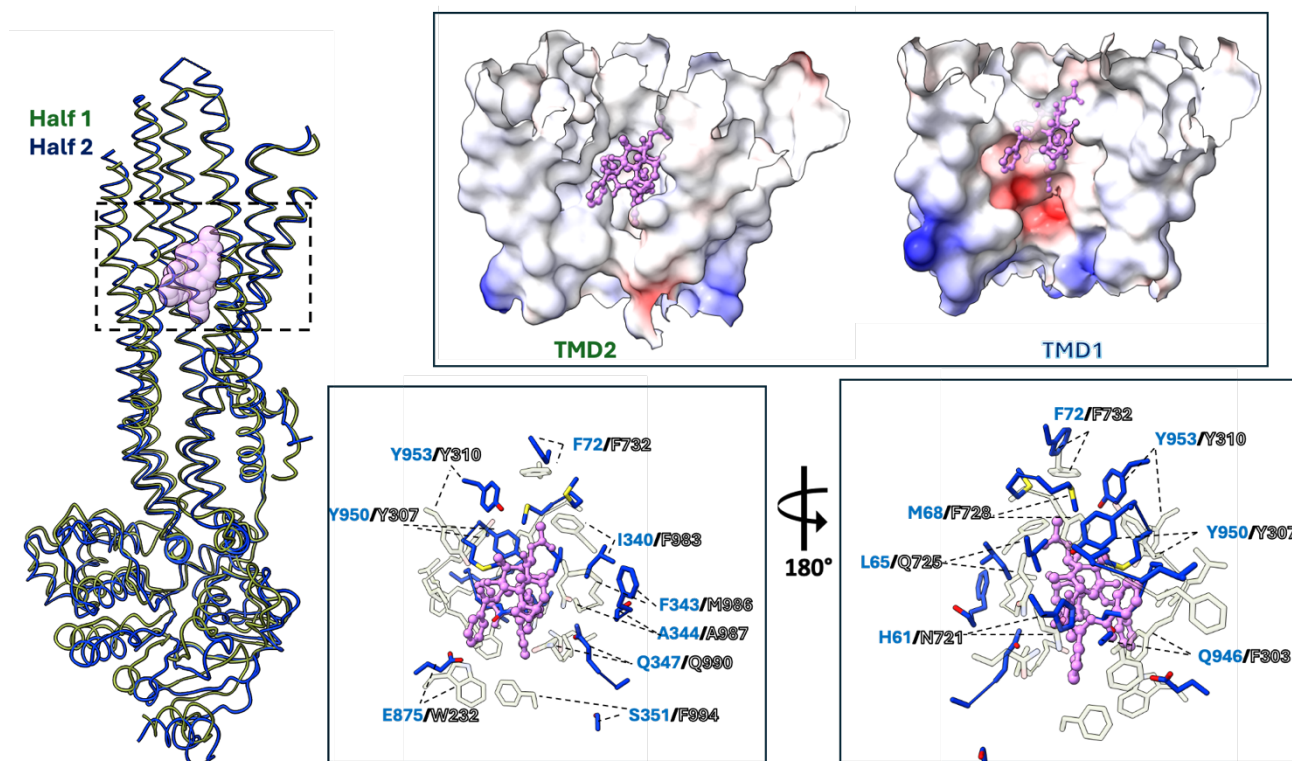molecules are shown as transparent spheres.

641

642

643

644

645

646

647

648

649

650   **Figure S2**

651

Figure S2 Mismatch between TMD1 and TMD2 cavities for taxol binding. **A** Overlay of domain swapped (DS) halves of ABCB1. The Taxol molecule bound to TMD2$_{DS}$ is shown as transparent pink spheres. The Zoom panel shows electrostatic potential map of the TMD2$_{DS}$ cavity (left) and its TMD1$_{DS}$ cavity equivalent (right) showing electrostatic and steric clashes with Taxol. **B** TMD1$_{DS}$ equivalent residues of TMD2$_{DS}$ residues (Blue sticks) within 5 Angstroms of bound Taxol (transparent sticks), with residue labels colored similarly.

652

653

654

655

656

657

658

659

660

661
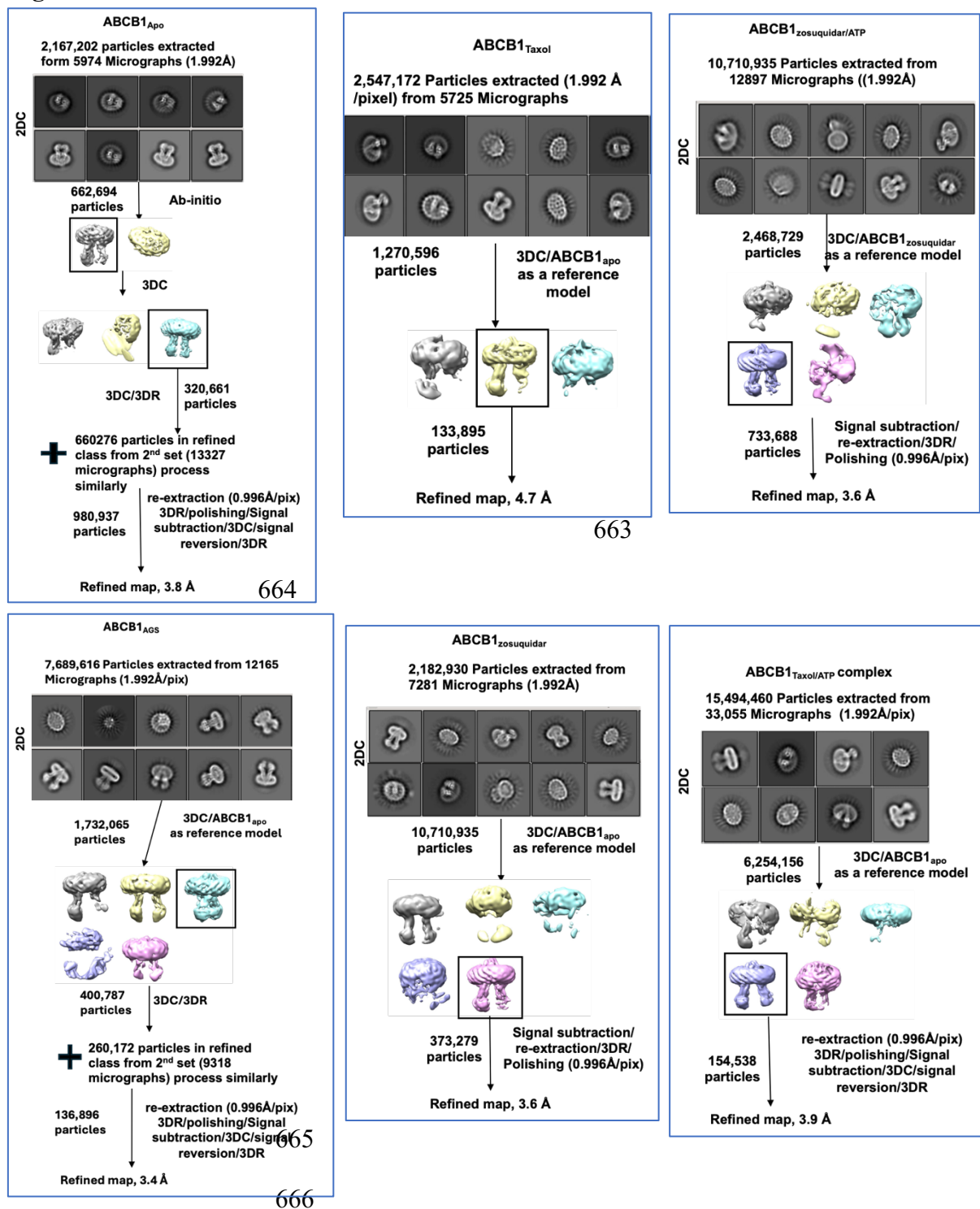
662 **Figure S3**

Figure S3 Data processing overview. 3D classes chosen for further processing are boxed.
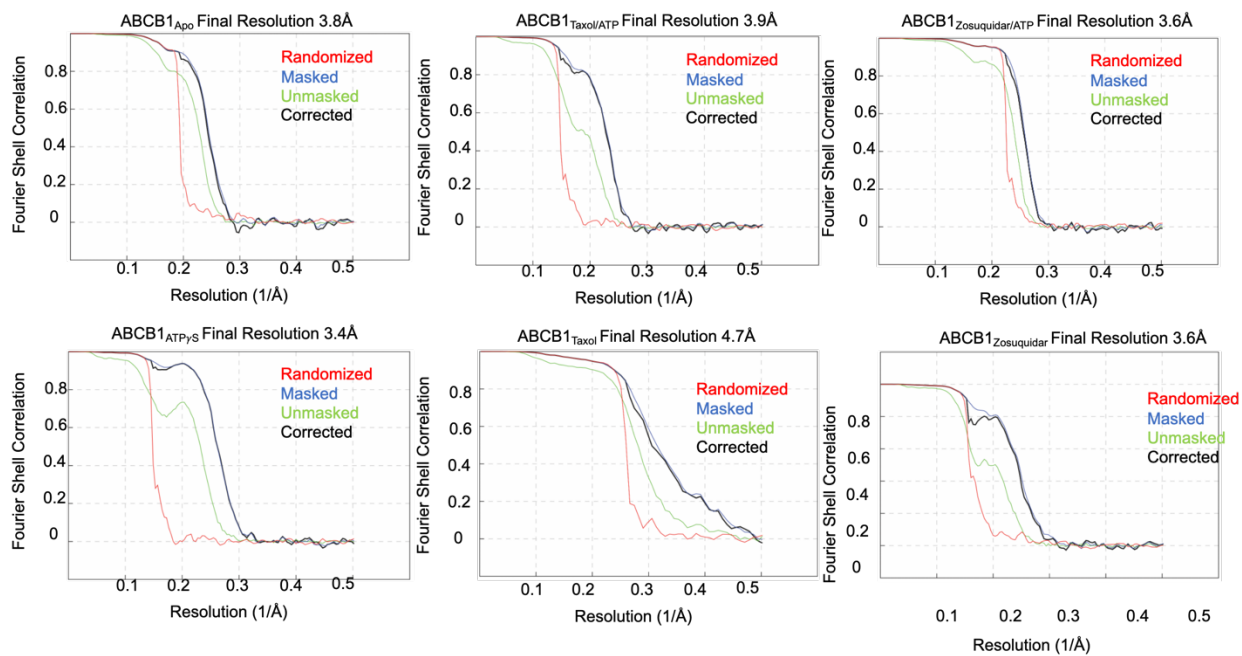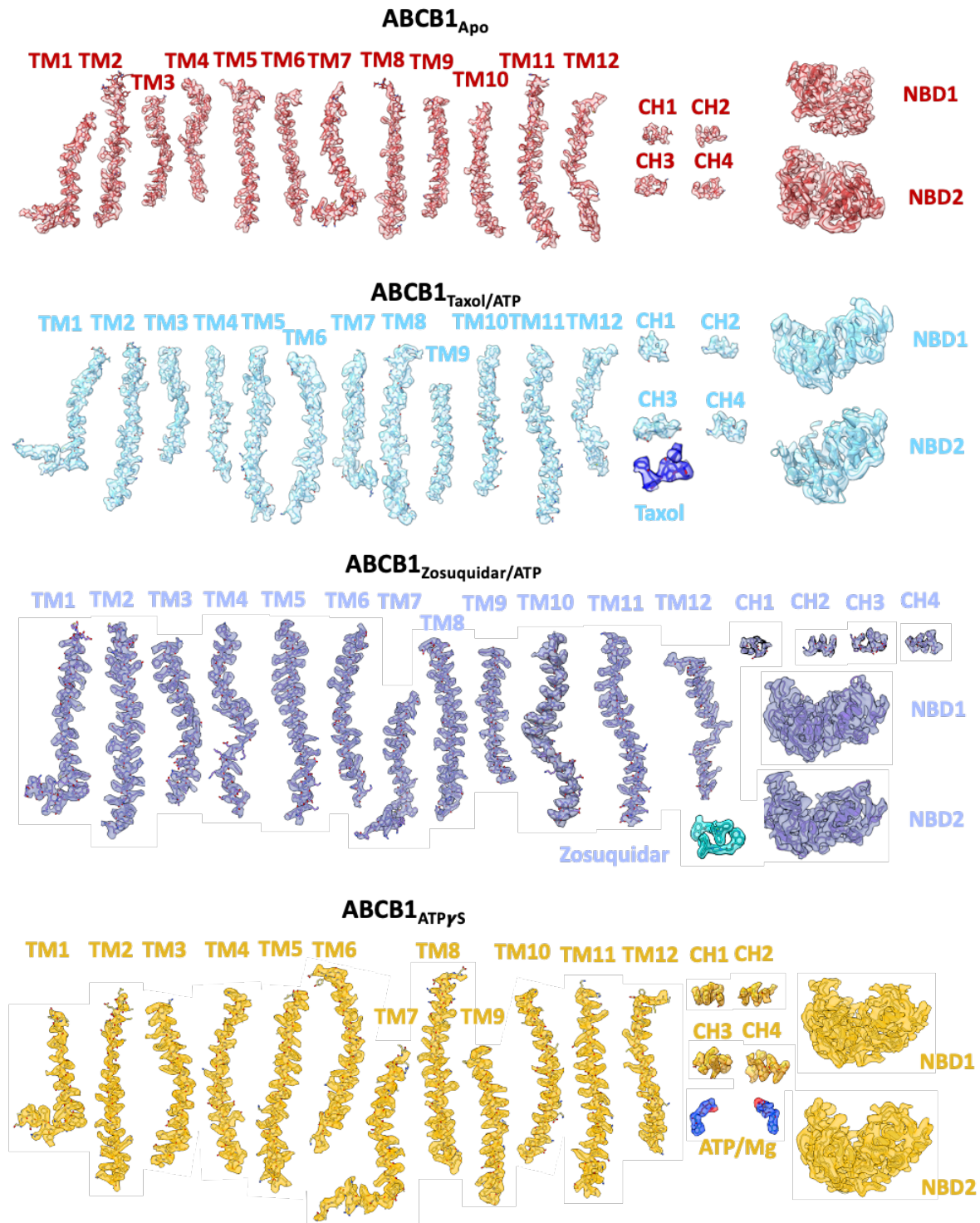
667

668

669 **Figure S4**

670

671

672

Figure S4 Data processing overview. FSC curves for final human ABCB1 maps
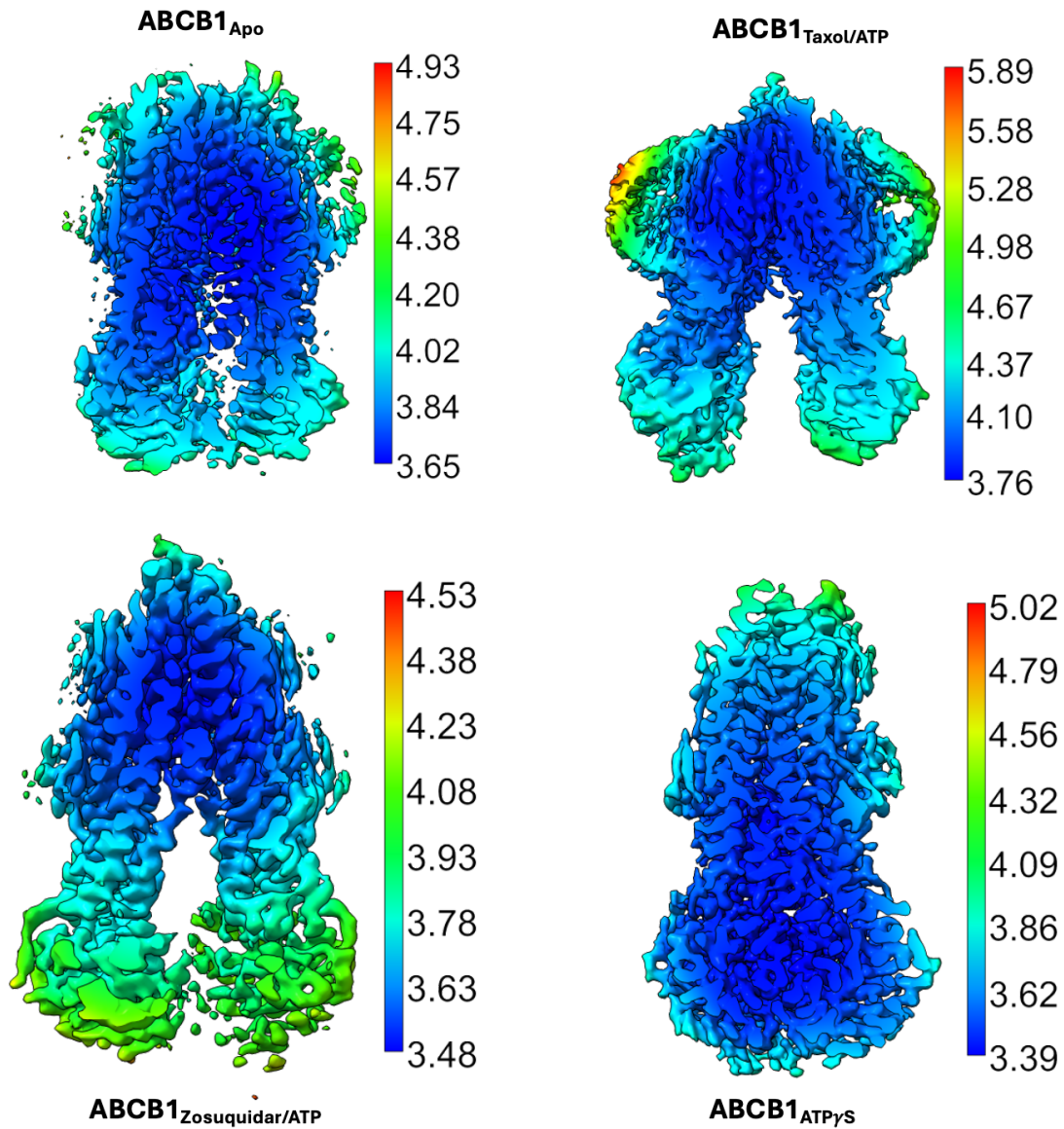
673 **Figure S5**

674

675 **Figure S5 EM Density maps for lipid embedded ABCB1**. Contour levels for Apo: 0.012; Taxol/ATP complex: 0.011; Zosuquidar/ATP complex: 0.031; and ATPγS complex:0.011

676

Figure S6 Local Density filtered Maps. Color Key indicates Resolution range for each filtered map.